# Giant piezoelectricity in oxide thin films with nanopillar structure

Huajun Liu[1,*,†], Haijun Wu[2,†], Khuong Phuong Ong[3], Tiannan Yang[4], Ping Yang[2,5], Pranab Kumar Das[5], Xiao Chi[6], Yang Zhang[2], Caozheng Diao[5], Wai Kong Alaric Wong[5], Eh Piew Chew[5], Yi Fan Chen[1], Chee Kiang Ivan Tan[1], Andrivo Rusydi[6], Mark B. H. Breese[5,6], David J. Singh[7], Long-Qing Chen[4], Stephen J. Pennycook[2], Kui Yao[1, *]

[1]Institute of Materials Research and Engineering, A*STAR (Agency for Science, Technology and Research), 2 Fusionopolis Way, 138634, Singapore.

[2]Department of Materials Science and Engineering, National University of Singapore, 9 Engineering Drive 1, 117575, Singapore.

[3]Institute of High Performance Computing, A*STAR (Agency for Science, Technology and Research), 1 Fusionopolis Way, 138632, Singapore.

[4]Department of Materials Science and Engineering, Pennsylvania State University, University Park, PA 16802, USA.

[5]Singapore Synchrotron Light Source (SSLS), National University of Singapore, 5 Research Link, 117603, Singapore.

[6]Department of Physics, National University of Singapore, 2 Science Drive 3, 117551, Singapore.

[7]Department of Physics and Astronomy, University of Missouri, Missouri 65211, USA.

*Correspondence to: huajunliu87@gmail.com; k-yao@imre.a-star.edu.sg

†These authors contribute equally.

**Abstract:** High-performance piezoelectric materials are critical components for electromechanical sensors and actuators. For more than 60 years, the main strategy for obtaining large piezoelectric response is to construct multiphase boundaries by tuning complex chemical compositions, where nanoscale domains with local structural and polar heterogeneity are formed. We used a different strategy to emulate such local heterogeneity by forming nanopillar regions in oxide thin films. We obtained a giant effective piezoelectric coefficient $d^*_{33,f}$ of ~1098 pm/V with a high Curie temperature of ~ 450 °C. Our lead-free composition of sodium-deficient sodium niobate contained only three elements (Na, Nb and O). Forming local heterogeneity with nanopillars in the perovskite structure could be a general approach to design and optimize various functional materials.

**One Sentence Summary:** Giant piezoelectric strain is obtained in lead-free thin films with nanopillar structure.

The well-established long-standing strategy for achieving high piezoelectric performance is to construct multiphase boundaries by tuning complex chemical compositions, such as the morphotropic phase boundary in lead zirconate titanate (PZT) (*1*) or the polymorphic phase boundary in potassium sodium niobate (KNN) (*2*). At these phase boundaries, energy differences among the distinct crystalline phases are adequately small with flattened thermodynamic energy profile, giving rise to low domain wall energy and miniaturization of ferroelectric domains (*3*, *4*). The local structural and chemical heterogeneity at the nanoscale is recognized to play a key role in achieving ultrahigh piezoelectric coefficients (*5*–*7*). However, the strategy of constructing composition-controlled phase boundaries usually involves complex chemical compositions, and these often have poor temperature stability due to a substantially reduced Curie temperature from extensive doping.

Defects like dislocations and dopants are important for developing materials with certain properties, such as the mechanical properties for metals or the electronic properties of semiconductors. An out-of-phase boundary is a type of extended crystallographic defect characterized by a misregistry of a fraction of a unit cell dimension in neighboring regions of a crystal (*8*). When the offset of the misregistry is a half of unit cell dimension, it is the special case known as the antiphase boundary (*8*, *9*). While the origins of out-of-phase boundaries and their influences on properties have been well studied in metal alloys (*10*) and semiconductor thin films (*11*), the investigation in complex oxides is rare (*9*) and its link to functional properties remains elusive (*8*). We show that the out-of-phase boundaries between the nanopillar regions and regular perovskite matrix induce local structural and polar heterogeneity and emergent giant piezoelectric response in lead-free, Na-deficient, $NaNbO_3$ thin films. We used atomic scale images to reveal the

formation of vertical nanopillars with size of a few to tens of nanometers. The structural distortions around nanopillar regions lower the crystal symmetry from tetragonal to monoclinic structure, facilitating polarization rotation and domain wall motion under electric fields to substantially enhance piezoelectric performance as supported by theoretical calculations. We discovered a giant effective piezoelectric coefficient $d^*_{33,f}$ of ~1098 pm/V at 1 kHz with an applied electric field of 125 kV/cm, which is more than twice that of the best PZT films (*12*) and four times that of the best KNN based films with extensive doping (*13*). We maintained a simple composition of three elements (Na, Nb and O) and a high Curie temperature of ~ 450 °C.

We grew epitaxial thin films of stoichiometric $NaNbO_3$ (NNO) with regular perovskite structure and Na deficient NNO with nanopillar regions (NPR-NNO) on Nb-doped $SrTiO_3$ (001) substrates by sputter deposition(*14*). Our stoichiometric NNO film was homogeneous with a thickness of ~200 nm, which we determined using low magnification annular bright field (ABF) image taken by scanning transmission electron microscopy (STEM) (Fig. 1A). The Nb atoms are arranged in a typical perovskite lattice (Fig. 1, B and C). In contrast, we found vertically aligned nanopillars with a smooth surface in the cross-sectional view of NPR-NNO film (Fig. 1D). Those nanopillars are embedded in the matrix of regular perovskite structure. Inside the nanopillar regions, the Nb atoms occupy the original Na positions along both in-plane directions (Fig. 1H), and the Na atoms also occupy the original Nb positions along both in-plane directions (fig. S2B). In the cross-section view (Fig. 1E), we observed many extended columnar structures. By changing the microscope focus we can confirm that these columnar structures are nanoscale in in-plane dimensions (fig. S1), fully consistent with the nanoscale size of nanopillar regions ranging from a few to tens of nanometers in the plan-view image (Fig. 1G). Because the thickness of the sample greatly exceeds the thickness of the nanopillars, we actually see overlapping of the nanopillar regions (marked by

arrows in Fig. 1E) and the matrix. The lattice in the nanopillar regions (yellow box in Fig. 1E and H) is shifted slightly by $\delta_C$ along the out-of-plane direction and approximately by a half unit cell along both in-plane directions from the lattice of the matrix (red box in Fig. 1E and H). Hence, the misregistry between the nanopillar regions and matrix can be seen as normal perovskite phase shifted by $\langle \mathbf{a}/2, \boldsymbol{b}/2, \boldsymbol{\delta}_C \rangle$, where $\boldsymbol{a}$ and $\boldsymbol{b}$ are unit vectors along in-plane directions and $\boldsymbol{\delta}_C$ is along the out-of-plane direction with magnitude of a small fraction of the unit cell length. This boundary is an out-of-phase boundary, which is different from an antiphase boundary where the displacement vector would be $\langle \mathbf{a}/2, \boldsymbol{b}/2, \boldsymbol{c}/2 \rangle$. Based on the above structure details, we constructed a schematic structural model (Fig. 1F and I). At the out-of-phase boundary between the nanopillar regions and the matrix, the oxygen octahedra are edge-sharing instead of the corner-sharing octahedra normally found in perovskites. Analogous to the Ruddlesden-Popper stacking faults in perovskites structure of $ABO_3$ with A-site excess (*15*), these out-of-phase boundaries can accommodate more Nb atoms than the stoichiometric perovskite (fig. S2). The Na deficiency (fig. S3) in the NPR-NNO film drives the formation of out-of-phase boundaries with atoms sitting at in-plane antisite positions (Fig. 1H and I). The interface atomic structure between the NPR-NNO film and the substrate (fig. S2g) shows that the first layer of film appears to be Nb occupied NaO layer, which largely determines the growth pattern of the nanopillar structures in the following layers. Based on first principles calculations (*14*), when Na is deficient and Nb is rich, the negative formation energy of antisite $Nb_{Na}$ shows that it is energetically favorable for excess Nb atoms to occupy Na vacancies.

We used synchrotron X-ray diffraction to investigate the crystal structures and temperature dependent phase transitions of the NNO and NPR-NNO thin films. The thickness fringes around

the main diffraction (001) peak of NPR-NNO film (Fig. 2A) reflect the high quality and smooth surface, while we observed no thickness fringes for NNO films. We found a single diffraction peak with the same in-plane lattice parameter as the Nb-STO substrate in the (103) reciprocal space mapping (RSM) for the NNO film (Fig. 2B). This indicates that the NNO film is coherently strained even at the thickness of 200 nm and the observation is consistent with a previous report (*16*). This is probably due to the small lattice mismatch of ~ 0.47% between the NNO bulk structure and the Nb-STO substrate (fig. S4). Combined with other RSMs, we found that the NNO film has a tetragonal symmetry. However, the (103) RSM for the NPR-NNO film (Fig. 2C) shows peak splitting due to monoclinic symmetry (see fig. S4 for more RSMs and lattice parameters). Oxygen octahedral rotations in the perovskite structure give rise to doubling of the unit cell along certain directions, which can be probed by the half-order diffraction peaks (*17*) (Fig. 2D). The half-order (0 0.5 1.5) diffraction peak is equivalent to the (0.5 0 1.5) peak (fig. S4b) due to the isotropic nature of the in-plane directions of the Nb-STO substrate, thus suggesting that the in-phase + rotation exists along both in-plane directions. Based on Glazer's notation (*18*), the rotation patterns for both films are a mixture of $a^-b^+c^-$ and $a^+b^-c^-$. However, the NPR-NNO film shows substantially lower peak intensity, especially the (1.5 0.5 1.5) and (0.5 0.5 1.5) peaks corresponding to out-of-phase rotations. This is probably due to the distortion induced by the nanopillar regions and the edge-sharing octahedra at the out-of-phase boundary (Figs. 1G-I) that breaks the long-range order of rotation.

We conducted temperature dependent X-ray diffraction was conducted to study the phase transition (Fig. 2E). The out-of-plane lattice parameter *c* shows a change in slope at ~457 °C for the NNO and NPR-NNO films. The changes in the in-plane lattice parameters *a* of both films are

less obvious, due to the constraint by the substrates. We also monitored the intensity of the half-order (0 0.5 1.5) diffraction peak (Fig. 2F). For both NNO and NPR-NNO films, the diffraction peaks disappear and the intensities decrease to the background level at ~457 °C. This observation suggests a phase transition from the $a^+$ and $b^+$ tilt pattern to non-tilted $a^0$ and $b^0$ of a higher symmetry phase with the likely space group being *P4/mbm* above 457 °C (*19*). Measuring the temperature dependence of the dielectric constant for the NPR-NNO film (Fig. 2G) shows a peak at ~ 450 °C, confirming the high Curie temperature. The smaller peak at ~ 210 °C could be related to a ferroelectric to ferroelectric phase transition, as we observed no obvious structural change (Fig. 2E and F). The hysteresis loops we measured demonstrate the ferroelectric nature of both films (fig. S5A-C).

We investigated the macroscopic piezoelectric properties of the films using a laser scanning vibrometer (*20–22*) with an AC unipolar voltage of 2.5 V in magnitude at 1 kHz for NNO film (Fig. 3A). We determined the effective piezoelectric coefficient $d^*_{33,f}$ to be ~22 pm/V based on the magnitude of the surface displacement. The electric field dependence of the piezoelectric coefficient and strain for the NNO film exhibits the linear dependence of strain on the electric field as found in typical piezoelectric materials (Fig. 3B). We found no dependence of the piezoelectric coefficient on the driving frequency of the electric field for the NNO film (Fig. 3C), which agrees with the impedance spectroscopy results (fig. S5D). We measured the film displacement of the NPR-NNO thin film under the same conditions as the NNO film (Fig. 3D). We determined the effective piezoelectric coefficient $d^*_{33,f}$ to be ~1098 pm/V at 1 kHz with an applied electric field of 125 kV/cm (Fig. 4E-F). The NPR-NNO thin film has non-linear behavior and much enhanced strain at a higher electric field (Fig. 3E). Decreasing the electric field leads to a very small strain

hysteresis of strain (Fig. 3E). This behavior departs from the strong hysteretic behavior of the point defect induced large strain in aged $BaTiO_3$ single crystal (*23*). The effective piezoelectric strain of the NPR-NNO thin film increases non-linearly with the electric field, saturating at ~1.4% above 125 kV/cm. We observed a strong dependence of the effective piezoelectric coefficient on the driving frequency of electric field for the NPR-NNO thin film (Fig. 3F). At a low frequency of 100 Hz, the effective piezoelectric coefficient reaches a giant value of ~ 8114 pm/V, while it drops to ~112 pm/V at a high frequency of 10 kHz. The strain shows a similar strong dependence on frequency (see fig. S6). We believe the strong amplitude and electric field frequency dependence of the piezoelectric strain of the NPR-NNO film indicates a substantial contribution from the motion of out-of-phase boundaries between nanopillar regions and the matrix perovskite (*24*). We observed a strong frequency dependence of dielectric constant and loss in NPR-NNO films in the impedance spectroscopy (fig. S5). X-ray absorption spectra (fig. S7**)** suggest a slightly occupied Nb 4d level in the NPR-NNO film as compared to the empty Nb 4d level in the NNO film, consistent with higher leakage in the NPR-NNO film (**Fig. S5f**) which could come from the vertical boundaries of the nanopillar regions.

We performed first principles calculations and phase-field simulations to better understand the mechanism of the giant piezoelectric response(*14*). We calculated the formation energy of antisite $Nb_{Na}$ defect as a function of chemical potential of Na under both Nb deficient and Nb rich conditions (Fig. 4A). The negative formation energy under Nb rich and Na deficient condition shows that excess Nb atoms would occupy Na vacant positions to form antisite $Nb_{Na}$ defects when NNO is Na deficient. However, due to large differences between ionic radius and valence of Na and Nb ions, antisite Nb atoms are not stable at the original antisite position but show substantial

off-centering along the out-of-plane *c* direction. This behavior is similar to Sr deficient $SrTiO_3$ thin films (*25*). First principle calculations predict the energies of antisite Nb atoms at different positions (Fig. 4B), showing that large off-centering displacement is energetically favorable. The off-centering displacement induces a large ferroelectric polarization of ~ 16.2 $\mu C/cm^2$ along the out-of-plane *c* direction in the structure with antisite defect. This polarization is greatly enhanced from the polarization of ~ 1.2 $\mu C/cm^2$ in the regular perovskite structure of NNO based on first principles calculations. This large local polarization distorts the surrounding lattice to lower symmetry, and gives rise to local structural heterogeneity at the nanoscale. However, the $d_{33}$ we calculated by first principles from the piezoelectric stress tensor and elastic stiffness (*14*) is ~17 pm/V for the structural model with antisite defect and ~ 14 pm/V for the structural model of normal perovskite. The similar values indicate that the giant strain we observed in the experiments likely originates at a scale beyond the unit cells of the lattice.

We employed phase-field simulations to study the contributions by nanopillar regions and their boundaries to the piezoelectric properties(*14*). We simulated the ferroelectric domain structure of the NPR-NNO film (figs. S9c-d). Due to the local stress developed around the boundaries of nanopillar regions (fig. S9e), the polarization directions are rotated away from the out-of-plane direction, thus forming a multidomain structure with coexisting tetragonal *c* domains and nanoscale monoclinic domains with rich and mixed orientations of polarizations. We simulated the piezoelectric strain response to a static electric field applied along the out-of-plane direction (Fig. 4C). The tetragonal domains (e.g., Region III in Fig. 4C) show a weak piezoelectric strain response while the monoclinic domains (e.g., Region I) show a much stronger response. The strongest piezoelectric strain response appears around the domain walls between tetragonal and

monoclinic domains (e.g., Region II). The motions of these domain walls under the electric field serve as substantial contributions to the piezoelectric response, giving rise to ~15 times enhancement of the piezoelectric coefficient $d_{33}$ ~ 290 pm/V for NPR-NNO film as compared with ~ 20 pm/V for pure NNO film from phase-field simulations. We simulated the frequency dependence of piezoelectric strain by applying an AC electric field at different frequencies (Fig. 4D). The domain wall motion is weakened upon increasing the frequency for the NPR-NNO film, (fig. S9f-h). The piezoelectric response of both the domain wall regions and the monoclinic domains decreases, while the piezoelectric response of the tetragonal domains is almost unchanged. For the NNO film with single tetragonal domain, the piezoelectric strain is almost independent of frequency. Our simulation results suggest that the giant piezoelectric response is likely to originate from domain wall motion under electric fields. The substantially reduced domain wall response at high frequencies results in the strong frequency dependence of piezoelectric property we observed.

Because the piezoelectric properties of ferroelectric materials are lost above the Curie temperature, a high Curie temperature $T_C$ is preferred for applications. We compare the piezoelectric coefficient $d_{33}$ of several major lead-free piezoelectric materials systems together with PZT ceramics as a function of Curie temperature $T_C$ (Fig. 4E, fig. S10A). A common strategy to enhance the piezoelectric coefficient in bulk ceramics is to construct phase boundaries by chemically tuning the composition. However, the complex chemical composition at the phase boundaries often reduces the Curie temperature (Fig. 4E). Our design strategy of constructing nanoscale structural and polar heterogeneity intrinsic to the nanopillar structure in NPR-NNO thin films has the advantage of improving the piezoelectric coefficient while simultaneously maintaining a high

Curie temperature (Fig. 4E). An additional advantage of the nanopillar approach is the simple chemical composition as compared with other thin films (Fig. 4F, fig. S10B). Complex chemical compositions make of phase boundary construction challenging as the dopant levels are only a few percent and often involve highly volatile elements (Na, K, Pb and Bi). This makes it challenging to get reliable and reproducible synthesis of bulk ceramics. Thin films are even more problematic to reliably synthesize. The NPR-NNO thin film contains only three elements, so our design strategy shows the great potential for improving composition control to obtain high performance piezoelectric thin films. Furthermore, because the out-of-phase boundary can be coupled to magnetic (*26*) and superconducting properties (*27*), forming local heterogeneity through such nanopillar structures in perovskite oxides ($ABO_3$) with A-site deficiency could enable other emergent phenomena in functional materials.

**References:**


1. B. Jaffe, W. R. Cook, H. Jaffe, *Piezoelectric ceramics* (Academic Press, New York, 1971).
2. J. Wu, D. Xiao, J. Zhu, Potassium–sodium niobate lead-free piezoelectric materials: past, present, and future of phase boundaries. *Chem. Rev.* **115**, 2559–2595 (2015).
3. W. Liu, X. Ren, Large piezoelectric effect in Pb-free ceramics. *Phys. Rev. Lett.* **103**, 257602 (2009).
4. J. Gao *et al.*, Microstructure basis for strong piezoelectricity in Pb-free $Ba(Zr_{0.2}Ti_{0.8})O_3$-$(Ba_{0.7}Ca_{0.3})TiO_3$ ceramics. *Appl. Phys. Lett.* **99**, 3–6 (2011).
5. F. Li *et al.*, Ultrahigh piezoelectricity in ferroelectric ceramics by design. *Nat. Mater.* **17**, 349 (2018).
6. Q. Liu *et al.*, High-performance lead-free piezoelectrics with local structural heterogeneity. *Energy Environ. Sci.* **11**, 3531–3539 (2018).
7. F. Li, S. Zhang, D. Damjanovic, L. Chen, T. R. Shrout, Local structural heterogeneity and electromechanical responses of ferroelectrics: learning from relaxor ferroelectrics. *Adv. Funct. Mater.* **28**, 1801504 (2018).

8. M. A. Zurbuchen *et al.*, Morphology, structure, and nucleation of out-of-phase boundaries (OPBs) in epitaxial films of layered oxides. *J. Mater. Res.* **22**, 1439–1471 (2007).

9. Z. Wang *et al.*, Designing antiphase boundaries by atomic control of heterointerfaces. *Proc. Natl. Acad. Sci.* **115**, 9485–9490 (2018).

10. M. J. Marcinkowski, N. Brown, R. M. Fisher, Dislocation configurations in $AuCu_3$ and AuCu type superlattices. *Acta Metall.* **9**, 129–137 (1961).

11. D. B. Holt, Antiphase boundaries in semiconducting compounds. *J. Phys. Chem. Solids*. **30**, 1297–1308 (1969).

12. M. D. Nguyen, E. P. Houwman, G. Rijnders, Large piezoelectric strain with ultra-low strain hysteresis in highly c-axis oriented $Pb(Zr_{0.52}Ti_{0.48})O_3$ films with columnar growth on amorphous glass substrates. *Sci. Rep.* **7**, 12915 (2017).

13. Y. Wang *et al.*, Outstanding Piezoelectric Performance in Lead-Free 0.95(K, Na)(Sb, Nb) $O_3$-0.05(Bi, Na, K)$ZrO_3$ Thick Films with Oriented Nanophase Coexistence. *Adv. Electron. Mater.* **5**, 1800691 (2019).

14. Materials and Methods are available as Supplementary Materials on Science Online.

15. R. J. D. Tilley, An electron microscope study of perovskite-related oxides in the Sr-Ti-O system. *J. Solid State Chem.* **21**, 293–301 (1977).

16. T. Saito, T. Wada, H. Adachi, I. Kanno, Pulsed laser deposition of high-quality (K,Na)$NbO_3$ thin films on $SrTiO_3$ substrate using high-density ceramic targets. *Jpn. J. Appl. Phys.* **43**, 6627 (2004).

17. A. M. Glazer, Simple Ways of Determining Perovskite Structures. *Acta Crystallogr. A.* **31**, 756–762 (1975).

18. A. M. Glazer, The classification of tilted octahedra in perovskites. *Acta Crystallogr. B.* **28**, 3384 (1972).

19. S. K. Mishra, N. Choudhury, S. L. Chaplot, P. S. R. Krishna, R. Mittal, Competing antiferroelectric and ferroelectric interactions in $NaNbO_3$: Neutron diffraction and theoretical studies. *Phys. Rev. B.* **76**, 24110 (2007).

20. K. Yao, F. E. H. Tay, Measurement of longitudinal piezoelectric coefficient of thin films by a laser-scanning vibrometer. *IEEE Trans. Ultrason. Ferroelectr. Freq. Control*. **50**, 113–116 (2003).

21. L. Wang, K. Yao, W. Ren, Piezoelectric $K_{0.5}Na_{0.5}NbO_3$ thick films derived from

polyvinylpyrrolidone-modified chemical solution deposition. *Appl. Phys. Lett.* **93**, 92903 (2008).

22. P. C. Goh, K. Yao, Z. Chen, Lead-free piezoelectric ($K_{0.5}Na_{0.5}$)$NbO_3$ thin films derived from chemical solution modified with stabilizing agents. *Appl. Phys. Lett.* **97**, 102901 (2010).
23. X. Ren, Large electric-field-induced strain in ferroelectric crystals by point-defect-mediated reversible domain switching. *Nat. Mater.* **3**, 91–94 (2004).
24. N. Bassiri-Gharb *et al.*, Domain wall contributions to the properties of piezoelectric thin films. *J. Electroceramics*. **19**, 47–65 (2007).
25. D. Lee *et al.*, Emergence of room-temperature ferroelectricity at reduced dimensions. *Science*. **349**, 1314–1317 (2015).
26. T. Hibma *et al.*, Anti-phase domains and magnetism in epitaxial magnetite layers. *J. Appl. Phys.* **85**, 5291–5293 (1999).
27. J. Orenstein, A. J. Millis, Advances in the physics of high-temperature superconductivity. *Science*. **288**, 468–474 (2000).
28. S. F. Ho, S. Contarini, J. W. Rabalais, Ion-beam-induced chemical changes in the oxyanions ($Mo_y^{n-}$) and oxides ($Mo_x$) where M= chromium, molybdenum, tungsten, vanadium, niobium and tantalum. *J. Phys. Chem.* **91**, 4779–4788 (1987).
29. X. J. Yu, C. Z. Diao, T. Venkatesan, M. B. H. Breese, A. Rusydi, A soft x-ray-ultraviolet (SUV) beamline and diffractometer for resonant elastic scattering and ultraviolet-vacuum ultraviolet reflectance at the Singapore synchrotron light source. *Rev. Sci. Instrum.* **89**, 113113 (2018).
30. J. P. Perdew *et al.*, Restoring the density-gradient expansion for exchange in solids and surfaces. *Phys. Rev. Lett.* **100**, 136406 (2008).
31. P. Blaha, K. Schwarz, G. Madsen, D. Kvasnicka, J. Luitz, WIEN2k: An Augmented Plane Wave plus Local Orbitals Program for Calculating Crystal Properties. *Tech. Univ. Wien, Wien*. **28** (2001).
32. S. B. Zhang, S.-H. Wei, A. Zunger, H. Katayama-Yoshida, Defect physics of the $CuInSe_2$ chalcopyrite semiconductor. *Phys. Rev. B*. **57**, 9642–9656 (1998).
33. S. Baroni, S. de Gironcoli, A. Dal Corso, P. Giannozzi, Phonons and related crystal properties from density-functional perturbation theory. *Rev. Mod. Phys.* **73**, 515–562 (2001).

34. Y. Le Page, P. Saxe, Symmetry-general least-squares extraction of elastic data for strained materials from ab initio calculations of stress. *Phys. Rev. B.* **65**, 104104 (2002).

35. X. Wu, D. Vanderbilt, D. R. Hamann, Systematic treatment of displacements, strains, and electric fields in density-functional perturbation theory. *Phys. Rev. B.* **72**, 35105 (2005).

36. L. Chen, Phase-field method of phase transitions/domain structures in ferroelectric thin films: a review. *J. Am. Ceram. Soc.* **91**, 1835–1844 (2008).

37. H. Pohlmann, J.-J. Wang, B. Wang, L.-Q. Chen, A thermodynamic potential and the temperature-composition phase diagram for single-crystalline $K_{1-x}Na_xNbO_3$ ($0 \leq x \leq 0.5$). *Appl. Phys. Lett.* **110**, 102906 (2017).

38. G. Rupprecht, R. O. Bell, Dielectric constant in paraelectric perovskites. *Phys. Rev.* **135**, A748 (1964).

39. I. Tomeno, Y. Tsunoda, K. Oka, M. Matsuura, M. Nishi, Lattice dynamics of cubic $NaNbO_3$: an inelastic neutron scattering study. *Phys. Rev. B.* **80**, 104101 (2009).

40. Y. L. Li, S. Y. Hu, Z. K. Liu, L. Q. Chen, Effect of electrical boundary conditions on ferroelectric domain structures in thin films. *Appl. Phys. Lett.* **81**, 427–429 (2002).

## ACKNOWLEDGEMENTS

**Funding:** The authors acknowledge the supports in part by Institute of Materials Research and Engineering, A*STAR, RIE2020 AME Core Funds - SERC Strategic Funds: Seeding R&D Activities for Competitive Grants (Grant number: A1718g0056), National Research Foundation Competitive Research Programme, NRF-CRP15-2015-04, and National Science Foundation (Grant number: DMR-1744213). H. Wu acknowledges Lee Kuan Yew Postdoctoral Fellowship through a Singapore Ministry of Education Tier 1 grant (R-284-000-212-114). S. J. P. and H. Wu are grateful to the Singapore Ministry of Education for a Tier 2 grant MOE2017-T2-1-129. We acknowledge the support of Singapore Synchrotron Light Source (SSLS) via NUS Core Support Grant C-380-003-003-001, which is a National Research Infrastructure under the National Research Foundation, Singapore. K. P. Ong acknowledge the support of Institute of High

Performance Computing, Agency for Science, Technology And Research (IHPC, A*STAR). Work at the University of Missouri (D.J.S.) is supported by the U.S. Department of Energy, Basic Energy Sciences, Award DE-SC0019114. H. Liu acknowledges helpful discussions with Dillon D. Fong and Hua Zhou. **Author contributions:** H. Liu conceived the main idea. H. Liu and C. Tan fabricated the ceramic targets. H. Liu grew the films. Y. Chen deposited the electrodes. H. Liu carried out the electric testing. H. Wu and Y. Zhang performed aberration-corrected STEM and analyzed the data. H. Liu, P. Yang, W. Wong, E. Chew performed X-ray diffraction and analyzed the data. P. Das, C. Diao and X. Chi carried out X-ray spectroscopy and analyzed the data. K. P. Ong performed DFT calculations and build theoretical models with the input from H. Liu and in discussion with D. J. Singh. Results of first principles calculations were analyzed by K. P. Ong and D. J. Singh. T. Yang and L. -Q. Chen performed and analyzed the phase-field simulations. K. Yao planned and guided the work, and analyzed the electric testing results. H. Liu, H. Wu, T. Yang, D. J. Singh, S. Pennycook, A. Rusydi, M. Breese and K. Yao wrote and modified the manuscript with inputs from others. All authors discussed the results and revised the manuscript. **Competing interests:** The authors have filed provisional Singapore Patent 10201908039P. **Data and materials availability:** All data are available in the main text and the supplementary materials.

**Supplementary Materials:**

Materials and Methods

Figures S1-S10

References 28-40

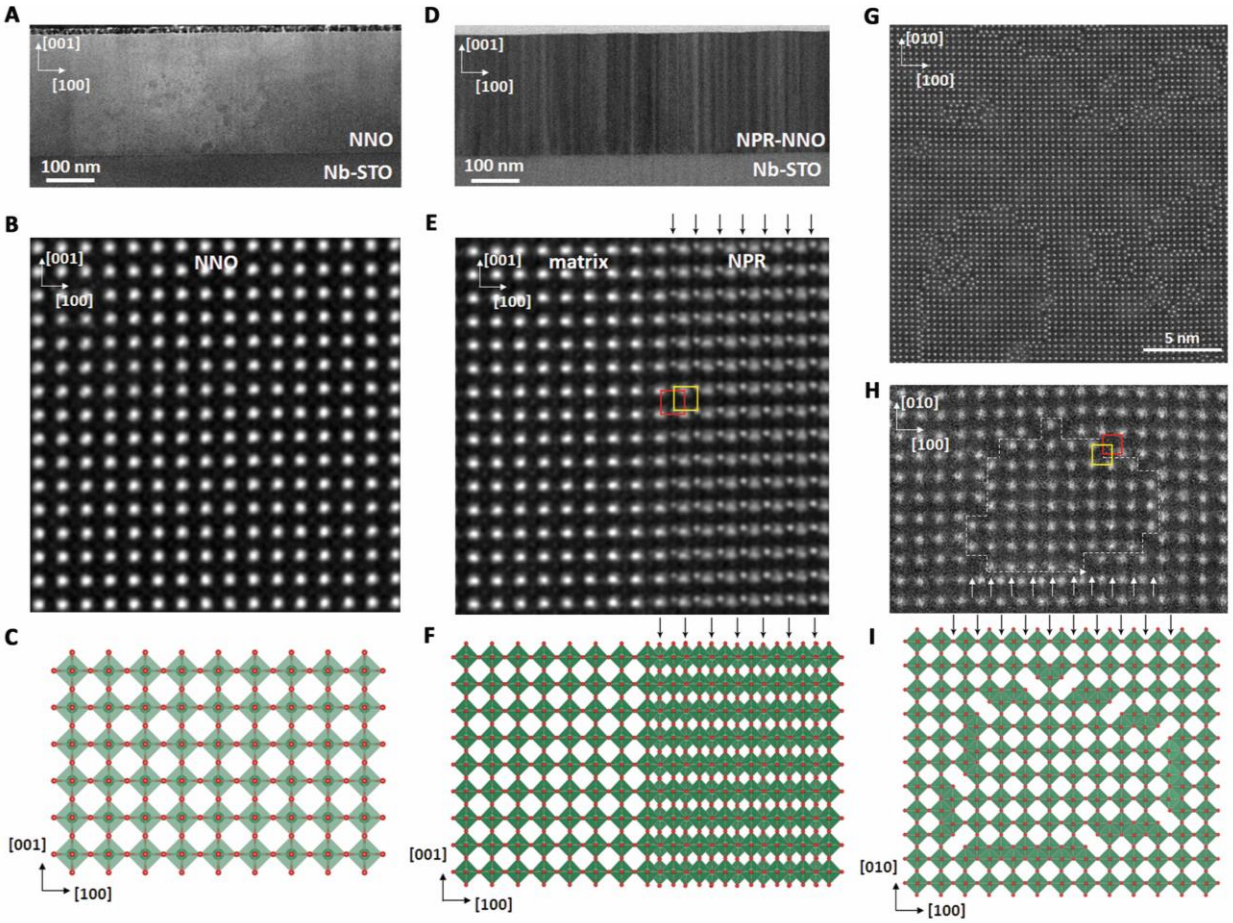


**Figure 1. Atomic structures of NNO and NPR-NNO thin films.** Cross-sectional low-magnification STEM ABF image (**A**), atomically-resolved HAADF image (**B**) and schematic structural model (**C**) of NNO thin films on Nb-STO (001) substrates. Cross-sectional low-magnification ABF (**D**) and atomically-resolved HAADF images (**E**), plan-view high-magnification image (**G**) and atomically-resolved HAADF image (**H**) of NPR-NNO thin films on Nb-STO (001) substrates. Schematic structural models of NPR-NNO films in cross-sectional (**F**) and plan view (**I**). The arrows in (**E**), (**F**), (**H**) and (**I**) indicate the rows of Nb atoms in the nanopillar regions. They are much weaker than the Nb atom columns in the normal crystal from cross-sectional view (**E**), because they are much shorter along the beam direction. The yellow and

red boxes in (**E**) and (**H**) represent the lattice of the nanopillar region and regular perovskite structure of matrix, respectively. The dashed lines in (**H**) show the nanopillar region.

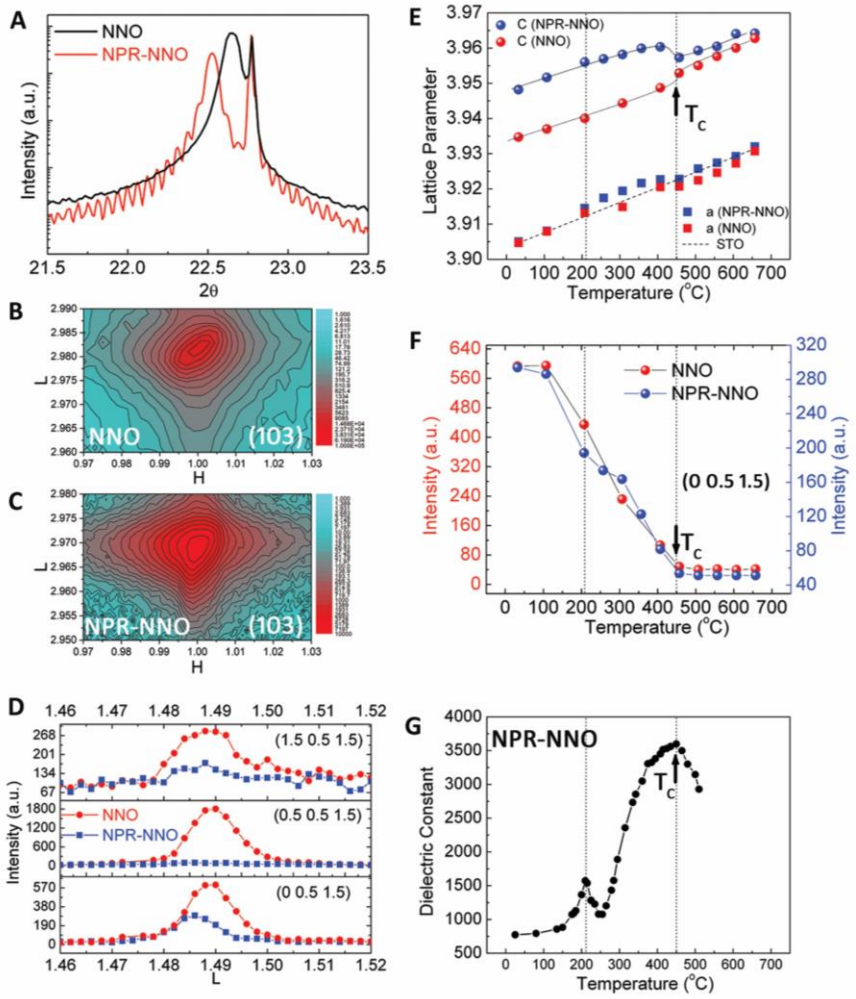


**Figure 2. Crystal structure and phase transition of NNO and NPR-NNO thin films.** (**A**), X-ray diffraction patterns around the (001) peak for NNO and NPR-NNO films. Reciprocal space mapping around the (103) peak for (**B**), the NNO film and (**C**), the NPR-NNO film, plotted in reciprocal lattice units of the Nb-STO substrate. (**D**), Half order diffraction peaks for the NNO and NPR-NNO film. (**E**), Lattice parameters of NNO and NPR-NNO films as a function of temperature. (**F**), Intensity of the half-order (0 0.5 1.5) diffraction peaks as a function of

temperature for NNO and NPR-NNO films. **(G)**, Dielectric constant measured at 1 kHz as a function of temperature for the NPR-NNO thin film.

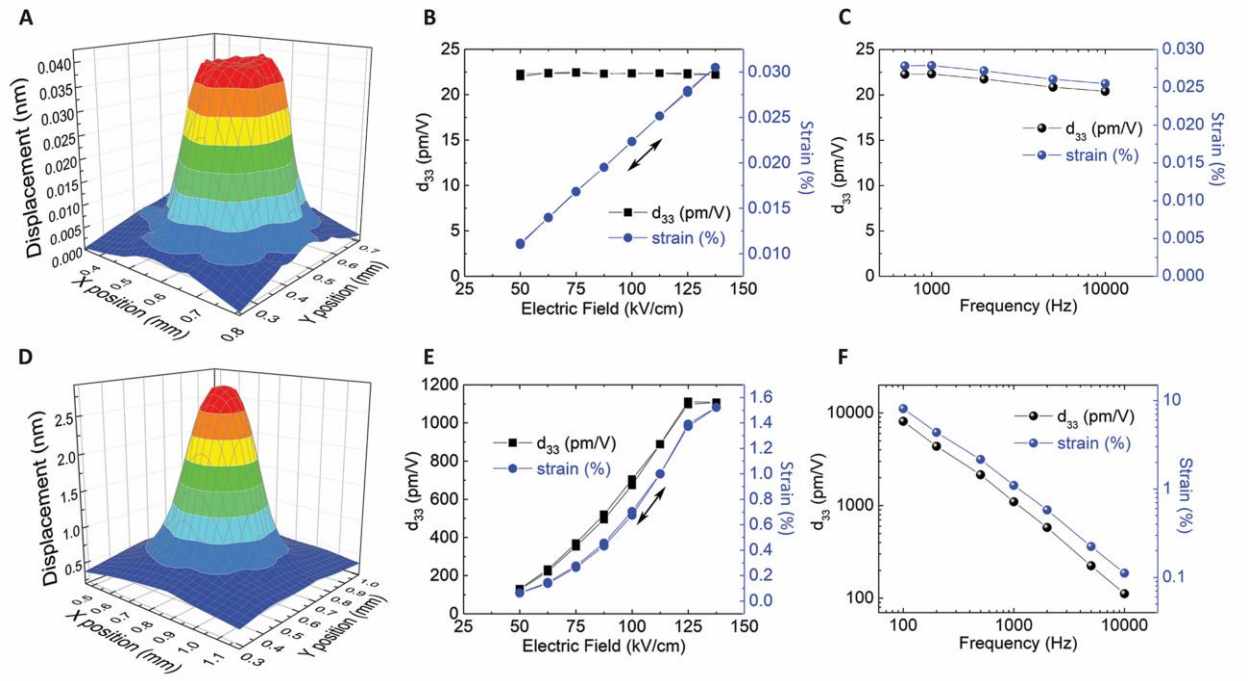


**Figure 3. Piezoelectric properties of NNO and NPR-NNO thin films.** 3D drawing of surface displacement of **(A),** NNO and **(D),** NPR-NNO film under AC unipolar voltage with 2.5 V in magnitude at 1 kHz. Electric field dependence of effective piezoelectric coefficient and strain of **(B)**, NNO and **(E)**, NPR-NNO film at the frequency of 1 kHz. Frequency dependence of effective piezoelectric coefficient and strain of **(C)**, NNO and **(F)**, NPR-NNO film measured under an AC unipolar voltage of 2 V in magnitude.

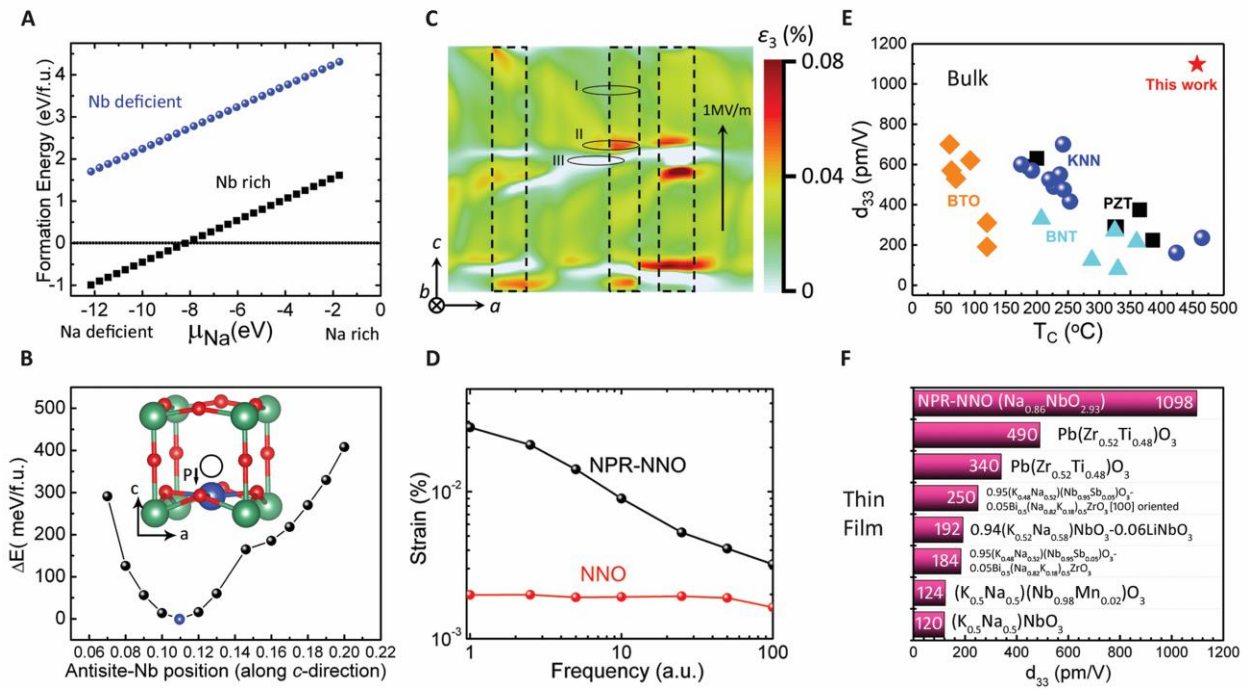


**Figure 4. Theoretical calculation and overview of piezoelectric properties. (A)**, Antisite formation energy as a function of chemical potential of Na under Nb rich and Nb deficient conditions. **(B)**, Energy curve of antisite Nb atom at different positions along the out-of-plane *c* direction. The structural model in the inset illustrates the off-centering displacement of antisite Nb atom (the blue sphere) in the lowest-energy position. The green spheres are regular Nb atoms and the red spheres are oxygen atoms. **(C)**, Mapping of the piezoelectric strain response of the NPR-NNO film under applied electric field of 1MV/m from phase-field simulation. Region I corresponds to the monoclinic domains, Region II the domain wall regions, and Region III the tetragonal domains. The dashed rectangles show the nanopillar regions. **(D)**, Average piezoelectric strain response of the NPR-NNO and NNO film as a function of field frequency from phase-field simulation. **(E)**, Comparison of piezoelectric coefficient $d_{33}$ of bulk material systems with this work (thin film) as a function of Curie temperature $T_C$. PZT: $Pb(Zr_{0.52}Ti_{0.48})O_3$ based piezoelectric materials, BTO: $BaTiO_3$ based piezoelectric materials, BNT: $(Bi_{0.5}Na_{0.5})TiO_3$ based piezoelectric

materials and KNN: $(K_{0.5}Na_{0.5})NbO_3$ based piezoelectric materials. **(F)**, Piezoelectric coefficient of the NPR-NNO thin film with simple chemical composition compared with other piezoelectric thin films with much more complicated chemical compositions.